



Full Length Article

Manufacturing and properties characterization of Ti patterned coatings for water electrolyzers by CSAM

Andrea Garfias^a, María Sarret^{a,b}, Javier Sánchez^a, Irene G. Cano^a,
Vicente Albaladejo-Fuentes^{a,*}, Teresa Andreu^{a,b}

^a Thermal Spray Center (CPT), Department of Materials Science and Physical Chemistry, Universitat de Barcelona, Carrer Martí I Franquès 1, 08028 Barcelona, Spain

^b Sustainable Electrochemical Processes, Department of Materials Science and Physical Chemistry & Institute of Nanoscience and Nanotechnology (IN2UB), Faculty of Chemistry, University of Barcelona, Martí i Franquès 1, 08028, Barcelona, Spain



ARTICLE INFO

Keywords:

Bipolar plates
PEM electrolyzers
Metal 3D printing
CSAM
Ti

ABSTRACT

This work investigates the microstructure and manufacturing control of the masked Cold Spray Additive Manufacturing (CSAM) strategy for producing of new bipolar plates (BPPs) for Proton Exchange Membrane (PEM) electrolyzers, using low-cost, lightweight, and machinable materials. CSAM is a solid-state process capable of fabricating 3D patterned parts based on a bottom-up approach using masks with a desired pattern. This study focuses on the dimensional and microstructural characteristics of pin fins fabricated with spherical (Ti-S) and irregular (Ti-I) Ti powders using the masked CSAM technology. Additionally, the performance of both Ti parts for its application in PEM electrolyzers was evaluated in terms of corrosion resistance and interfacial contact resistance (ICR). The results demonstrated that the masked CSAM technology allowed precise control and customization of the dimensions of the 3D-printed pin fins, obtaining porosity values of $6 \pm 1\%$ for Ti-S and $4 \pm 1\%$ for Ti-I. The evaluation of the corrosion resistance of the CSAM Ti patterned parts showed that for both Ti-S and Ti-I powders a stable oxide film at the typical operation potential (1.8 V vs Ag/AgCl) of a PEM water electrolyzer was formed without signs of pitting corrosion. Finally, at a compaction pressure of 150 N/cm² ICR values of 42 ± 19 , 40 ± 13 , and 24 ± 7 mΩ·cm² were obtained for Ti-I, Ti-S, and standard Ti Bulk, respectively. The results suggest that the masked CSAM technology shows great potential for the fabrication of Ti BPPs.

1. Introduction

Hydrogen is well known to serve as a carrier gas and has emerged as a highly effective and promising energy storage method. Due to its scarcity in its elemental state, its production usually needs an energy input. As a result, it is primarily considered a secondary energy carrier, derived from either renewable sources (such as wind, solar, geothermal) or non-renewable sources (such as coal, gas, and nuclear). The ability to store hydrogen as a portable and accessible fuel represents a significant advancement in the field of energy sustainability, addressing one of the world's key environmental challenges: meeting the increasing demands of electricity generation [1,2]. Today, the cheapest way to produce it is by means of steam reforming of natural gas or gasification of fossil fuels, both methods leading to a considerable production of CO₂ as a by-product [3,4].

A promising alternative method for hydrogen production is through

the electrochemical splitting of water with electrolyzers. This technology is powered by renewable sources, wherein electrical energy is applied to promote a reaction that separates H₂O molecules into H₂ and O₂. The resulting purity of H₂ from this process is typically close to 100% [4–6]. There are three main types of water electrolysis technologies: alkaline water electrolyzers (AWE), polymer electrolyte membrane (PEM), and solid oxide electrolysis cells (SOEC), currently being the AWE the most well established and mature technology [7]. The operation principle of these electrolyzers is different for each of them. Particularly, the PEM water electrolyzers are composed of several parts: two terminal end plates, bipolar plates (BPP), gas diffusion layers (GDL) and a PEM placed at the center, as shown in Fig. 1.

In PEM electrolyzer cells, water is introduced into the anodic part of the cell, where it is uniformly distributed by the anodic BPP and comes in contact with the GDL and the PEM. Upon applying an electric current to the cell, a potential difference is established, acting as the driving

* Corresponding author at: Thermal Spray Center (CPT), Department of Materials Science and Physical Chemistry, Universitat de Barcelona, Carrer Martí I Franquès 1, 08028 Barcelona, Spain.

E-mail address: vicente.albaladejo@ub.edu (V. Albaladejo-Fuentes).

<https://doi.org/10.1016/j.apsadv.2024.100649>

Received 10 July 2024; Received in revised form 1 October 2024; Accepted 13 October 2024

Available online 25 October 2024

2666-5239/© 2024 The Authors. Published by Elsevier B.V. This is an open access article under the CC BY-NC license (<http://creativecommons.org/licenses/by-nc/4.0/>).

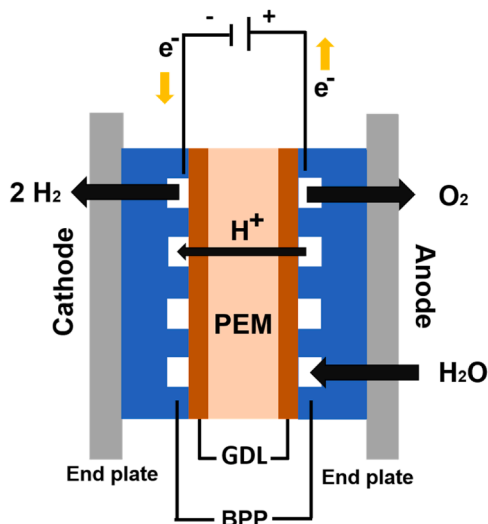
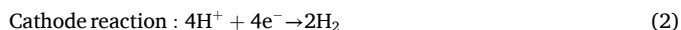


Fig. 1. PEM electrolyzer cell components.

force for a redox reaction to occur. At the anode, the oxidation of water takes place, while at the cathode the reduction of protons occurs to form hydrogen gas. These reactions are described as follows:



The proton exchange membrane, usually made of a thin layer of polymer membrane of perfluorosulfonic acid (PFSA) acts as a selective barrier, allowing only for protons (H^+) to flow from the anode to the cathode. The electrons are directed through an external circuit and create an electric current. At the cathode, the protons and the electrons recombine to form H_2 gas [7].

While the potential of producing green hydrogen through PEM water electrolyzers is promising, their use in industry and large-scale production has been limited by their high costs. Specifically, BPPs contribute for 80 % of the cell's weight, and account for approximately 40–60 % of its total cost [8]. As a result, there is a need to develop new BPPs produced with low-cost, lightweight, and easily manufacturable materials while ensuring they possess the specific properties required for an efficient operation [9,10].

The BPPs are required to have characteristics that are highly restraining and might be contradictory, such as to be chemically and mechanically stable, while being resistant to corrosion and electrically conductive [7,9,10]. The previous target of the U.S. Department of Energy (DOE) initiative for 2020 determined the technical parameters required for the BPP materials, including an interfacial contact resistance (ICR) $< 10 \text{ m}\Omega\cdot\text{cm}^2$ and a corrosion resistance $I_{\text{corr}} < 1 \mu\text{A}$.

Currently, titanium and stainless steels (SS) are considered the most promising metals for the production of cost-effective BPPs, due to their excellent mechanical properties, resistance to corrosion, and suitability for large-scale production [9]. However, these materials also present certain challenges that need to be addressed. Ti is notoriously difficult to machine, making manufacturing through the BPPs conventional manufacturing methods such as machining or stamping difficult [11]. Therefore, other manufacturing methods such as additive manufacturing offer a potential solution. On the other hand, SS is susceptible to corrosion in acidic media, particularly at anodic potentials. Consequently, SS BPPs are usually coated with a more noble material such as Nb or Au [12–15].

Some studies investigate the possibility to manufacture metallic BPPs with additive manufacturing (AM), however there is still a need to explore and optimize the different technologies for a cost-effective production of high-performance BPPs [16]. On one hand, few studies

are focused on the manufacturing and characterization of Ti BPPs [17–19]. Lyons et al. [17] and Celik et al. [18] manufactured Ti BPPs using Direct Metal Laser Sintering (DMLS) and Selective Laser Sintering (SLS) AM technologies, respectively. However, both studies coated the parts with an additional corrosion resistant coating, increasing the final price of the 3D printed parts [20]. Moreover, Romero et al. [19] manufactured Ti BPPs using powder metallurgy routes, and improved the final part's performance through a gas nitriding treatment. On the other hand, more studies that investigate fabrication AM processes of SS BPPs are found in the literature. For instance, Yang et al. [21] successfully demonstrated the viability of manufacturing a cathode SS 316 L plate using selective laser melting (SLM), indicating that additive manufacturing (AM) could be a rapid and cost-effective approach to develop BPPs. Additionally, Yang et al. [22] conducted further research on the aforementioned BPPs, coating them with a protective layer of Au through electroplating. This additional step allowed the BPPs to withstand the aggressive acidic conditions to be implemented on both the anodic and cathodic sides of the electrolyzer cell. Furthermore, Huang et al. [23] also utilized SLM to manufacture bipolar plates using SS 316 L material. The authors fabricated the BPPs with various flow-fields and evaluated their efficiencies through computational fluid dynamics (CFD) simulations, concluding that the BPPs produced by SLM showed high forming quality. On the other hand, Sánchez-Molina et al. [24] manufactured SS 316 L BPPs by powder bed fusion (PBF), and compared their properties with bipolar plates manufactured by conventional machining processes, both parts showed similar characteristics in ex-situ corrosion tests, exhibiting PBF as a potential AM technology for the production of BPPs.

Since only a few studies have investigated a manufacturing methodology of Ti BPPs, and no works are reported on the literature on the fabrication of BPPs with thermal spray techniques, in this study a methodology to manufacture Ti BPPs with cold spray additive manufacturing (CSAM) is developed. CSAM is a solid-state process that involves propelling a powder feedstock inside a gun using preheated, compressed, supersonic gas (N_2 or H_2) at high velocities ($300\text{--}1200 \text{ m s}^{-1}$) through a convergent-divergent (de Laval) nozzle. When the accelerated powder impacts a substrate with sufficient kinetic energy, it undergoes plastic deformation at the point of impact, leading to particle adhesion. With this technology, bipolar plates of different materials can be built (such as Cu, Al, SS 316 L, and Ti) with customized flow-fields. Since it is a bottom up approach and a solid-state technology, problems such as machinability and undesired phases and oxidation in the plates are avoided.

The objective of this work is to develop a manufacturing process for Ti patterned parts using masked CSAM and to evaluate the dimensional and microstructural characteristics of irregular (Ti-I) and spherical (Ti-S) parts. Additionally, this study evaluates the behavior and performance of the CSAM Ti deposits in aggressive environments, focusing on their corrosion resistance in acidic media and interfacial contact resistance (ICR) as required for the commercial BPPs used in PEM electrolyzers.

2. Materials and methods

2.1. Feedstock powder characterization

Two titanium powders with notable cost differences are investigated in this work: a low-cost Ti powder (CNPC powder), characterized by irregular morphology and produced through the pulverization of Ti sponge material, and a comparatively more expensive gas-atomized Ti powder (AP&C), featuring spherical particle shapes. In this study both powders are labeled as Ti-I and Ti-S, respectively.

The particle morphology of each powder was observed in a Phenom ProX Desktop scanning electron microscope (SEM). The powder size distribution was determined with a laser diffraction particle sizing analyzer LS 13 320 Model Dry Powder System.

2.2. Bipolar plates manufacturing and process parameters

Both powders were sprayed with the high pressure CGS equipment Plasma Giken PCS 100 on grit-blasted steel substrates with a 1.5 mm thickness, with the spraying parameters indicated in Table 1.

The BPPs manufacturing methodology is based on selectively shielding the substrate from deposition with a pattern that resembled the inverse of the geometry to be deposited, being in this case the flow field channels of the BPP. While spraying, the particles are able to flow through the selected geometry and deposit forming a 3D pattern. This masking process is schematically shown in Fig. 2. Thus, Ti 3D patterned coatings were manufactured by using laser-cut steel mesh masks with different patterns: big squares (mesh with squared holes 3×3 mm), small squares (mesh with squared holes 1.5×1.5 mm), rows, and cylinders. The masks were placed between the gun and the steel substrate, allowing the powder to flow through the voids and to form the 3D flow fields of the plates. The mask-substrate distance was systematically optimized to attain homogeneity and precise control of the titanium deposits geometry via CSAM. This masking methodology was developed by Cormier et al. [25], where the authors used a mask for depositing aluminum and stainless steel 304 L pin fins in aluminum substrates.

Particularly, for the manufacturing of the BPPs, a substrate is coated with the spraying of a base layer that acts as the bottom surface of the flow-field. Then, a mesh cut with the inverse of the desired pattern is attached to the plate for a second spray that builds up the pin fins that form the flow-field of the plates. Finally, the attached mesh is removed to obtain the final BPPs. The first two steps are shown in Fig. 3.

2.3. Microstructure, mechanical properties & adhesion

The microstructural characterization and the mechanical properties of the BPPs with both powders were determined. The metallographic preparation of all samples was completed according to the standard ASTM E1920–03(2014). The cross-sectional surface of the polished samples was analyzed with the optical microscope (OM) Leica DMI5000M. The mean porosity was calculated using image analysis software ImageJ (v. 153e) according to the standard ASTM E2109–01 from 10 cross-sectional OM images at 20x magnification. The profilometer SJ-210 Mitutoyo was used to obtain the superficial roughness of the BPPs. The Vickers microhardness was calculated from 10 indentations for each sample, following standard ASTM E384–17 with 0.2 kgF using Shimadzu HV-2/HMV-2T equipment.

The adhesion of the deposits with the substrate was tested with equipment SERVOSIS ME 402–10 following the ASTM C633–13 standard. Three samples of each material were evaluated by adhering them to a grit-blasted counterpart with the adhesive HTK Ultrabond 100; a tensile test at a rate of 0.01 mm s^{-1} was performed until failure.

2.4. Bipolar plates profile & 3D topography

To evaluate the dimensions and superficial characteristics of the different patterns, the profilometry of the samples, along with their 3D topography was evaluated with confocal microscope Sensofar Plu2300.

2.5. Electrochemical experiments

The corrosion resistance of sprayed materials was tested by subjecting a 1 cm^2 sample to electrochemical measurements under similar

Table 1
Feedstock powders and cold gas spraying parameters.

Label	Feedstock powder	Pressure (bar)	Temperature (°C)	Standoff distance (mm)
Ti-I	Ti (CNPC)	60	900	40
Ti-S	Ti (AP&C)	60	900	40

conditions to those experimented in the anodic side of an operating PEM electrolyzer. The experiments were performed in a 0.5 M H_2SO_4 solution with oxygen saturation. To assess the corrosion behavior, polarization curves were recorded using a VSP potentiometer. The polarization curves were generated by varying the potential from -100 to 2400 mV compared to the open circuit potential (E_{OCP}). Subsequently, Tafel fit extrapolation method was evaluated with EC-Lab software (V10.44) to determine E_{corr} (corrosion potential) and I_{corr} (corrosion current). These potentials were chosen to show the corrosion properties of both powders within the potential range of an operating PEM electrolyzer.

To assess the stability of the materials, they were immersed in a 0.5 M H_2SO_4 solution and subjected to a constant potential of 2 V for 100 h . The E_{corr} and I_{corr} were measured both before and after the stabilization test. Subsequently, all samples evaluated after the stability test are referred to as "post-mortem" samples.

2.6. Interfacial contact resistance

The powders were cold-sprayed onto both sides of a 9 cm^2 steel substrate with 1 mm of thickness. The sprayed samples were subsequently grinded on both sides with a 120 SiC paper until 1 mm of Ti coating remained on each side. To determine the interfacial contact resistance (ICR), the approach proposed by Wang et al. [26], based on the Davies' method [27], was employed. In this modified method, the ICR was measured in two setups: first, the Ti sample was placed between two pieces of Toray conductive carbon paper and two copper plates, and second, only one piece of Toray paper was inserted between the copper plates. The final ICR was calculated with the ICR difference of both setups.

For this, a compaction force ranging from 0.25 to 2 kN/cm^2 was applied using the SERVOSIS ME 402–10 equipment. For each setup and compaction force, a current of 1 A was passed (between the copper plates) using the DC power supply LABPS1503. The voltage drop across the system was measured using the HP 3458A multimeter and calculated employing Ohm's law Eq. (3).

$$R = \frac{VA_s}{I} \quad (3)$$

The ICR was measured before and after the post-mortem experiment.

3. Results and discussion

3.1. Feedstock powder

The selection of the feedstock powder in the CS process is of vital importance, as it not only affects the properties of the final deposit, but also has a great influence on the total cost of the process [28]. In addition, the morphology and particle size distribution of the powders are key factors influencing the deposition efficiency and the final quality of the coatings. Fig. 4 and Table 2 show the SEM micrographs, as well as the mean particle size of both powders, respectively. The SEM micrographs exhibit the morphology for both powders. As expected, powder Ti-I exhibited irregular particles, while powder Ti-S showed spherical particles. These images also show the variation of the particle sizes. Despite both powders having a similar mean particle size, Ti-I presented a broader size distribution compared to Ti-S, which could impact the shape of the deposits due to the deflection of large particles with the mesh.

Some studies have focused on evaluating the effects of powder morphology on coating properties such as porosity, microhardness, mechanical properties and deposition efficiency [29,30]. Vaz et al. [29] evaluated the properties of SS 316 L CS coatings sprayed with different powders under the same conditions. Their findings indicated that there is no distinct advantage to using spherical powder over irregular powder in terms of coating quality, mechanical properties, resistance to corrosion, and resistance to abrasive conditions. Furthermore, Wong et al.

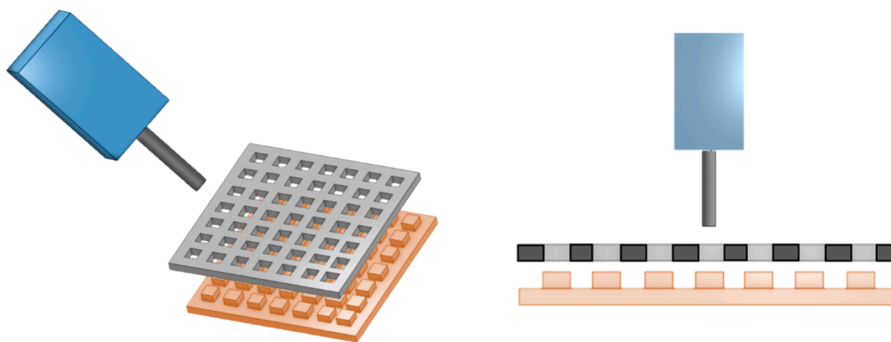


Fig. 2. CSAM masking process.

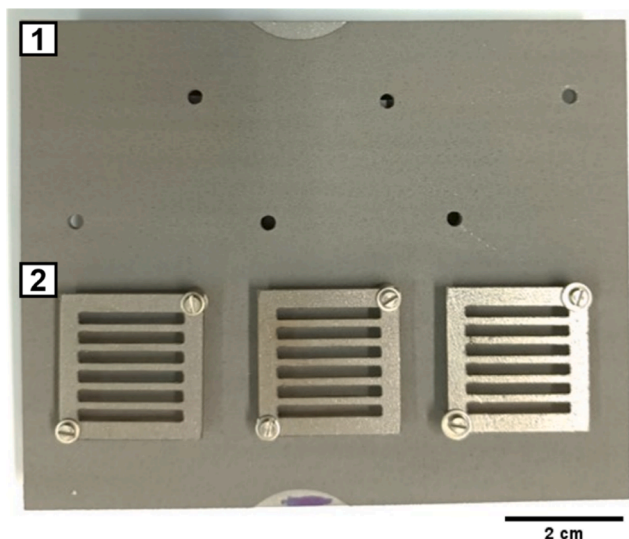


Fig. 3. Masked CSAM process steps: (1) Ti base layer and (2) mesh setup.

[30] investigated the influence of different morphologies of pure Ti powder on coating properties. Although their results demonstrated that spherical powder exhibited the highest deposition efficiency, the irregular powder showed similar porosity values to those of the spherical powder. Consequently, spraying irregular powders can produce coatings with characteristics very similar to those of spherical powders under the optimal spraying conditions, with the added advantage of being more

cost-effective.

3.2. Bipolar plates profile & 3D topography

One of the major problems of the large-scale production of PEM electrolyzers is the high costs of the BPPs. Since these plates require a material that can withstand aggressive acidic conditions, while being able to be electrically conductive, only a few materials are good candidates [4]. In general, metallic BPPs are commonly produced through methods such as stamping, hydroforming, and milling [31]. Nonetheless, these processes further limit the range of materials that can be effectively used, including titanium, due to its limited ductility at room temperature [32]. This limitation affects the accurate production of BPP with flow field channels in the range of hundreds of microns. As mentioned before, there are only a few studies available in the literature regarding the additive manufacturing of BPPs, and none of them specifically explore titanium.

Fig. 5 shows the resulting Ti patterned surfaces produced by CSAM that correspond to the flow field channels of a BPP. As previously indicated, four different patterns were investigated in this study starting from squared flow-fields of different dimensions (Fig. 5A-B), up to other patterns composed of rows or cylinders (Fig. 5C-D).

Table 2
Mean particle size of the feedstock powders.

Powder	Shape	Mean particle size (μm)	d10 (μm)	d90 (μm)
Ti-I	Irregular	40.1 ± 2.8	9.7 ± 0.8	89.5 ± 6.4
Ti-S	Spherical	36.2 ± 2.2	20.8 ± 3.1	56.4 ± 4.4

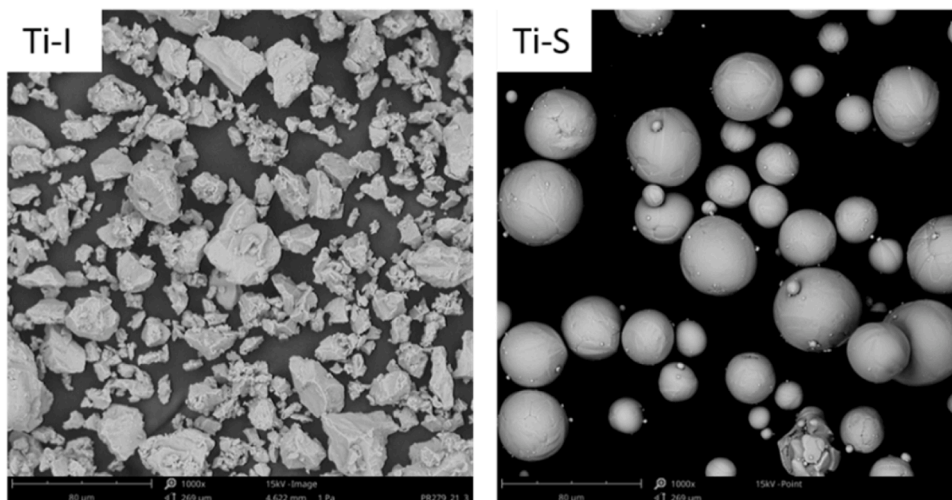


Fig. 4. SEM micrographs of the powders.

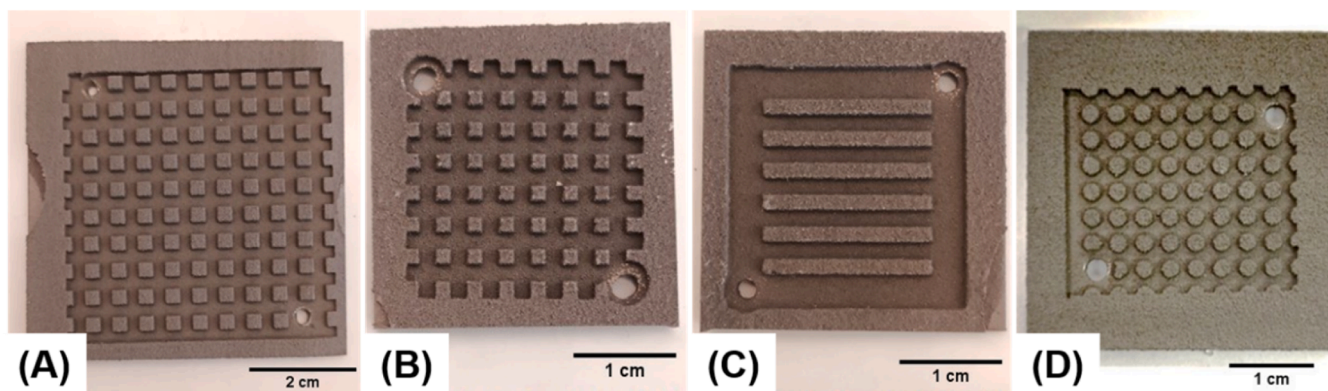


Fig. 5. CSAM BPPs with different flow-field patterns. (A) big squares, (B) small squares, (C) rows, (D) cylinders.

The importance of the accurate manufacturing of the flow field channels lies on the crucial role that the design of the flow-field plays in optimizing the operation efficiency of the PEM electrolyzers. Particularly, the BPPs not only act as a conductive and support component of the PEM electrolyzers but they should distribute and maintain a uniform flow throughout its surface. Achieving a uniform flow helps to reduce the internal cell resistance and to prevent the risk of localized corrosion [33]. For this reason, BPPs with several patterns and sizes were sprayed in this work.

In addition to the flow-field design, achieving homogeneity in the 3D printed pins is essential to maintain an optimal contact with the gas diffusion layers, thereby minimizing the interfacial contact resistance and ensuring a uniform pressure in the cell [34]. To assess the homogeneity of the Ti deposits by CSAM, the 3D topography and the profile characteristics of the pins were evaluated using confocal microscopy. Fig. 6 shows the flow-field dimensions exhibited by the 3D topography

evaluation. Overall, the pins were uniformly distributed with similar heights, regardless of the pattern. However, it was observed that, in all cases, the pins tended to grow exhibiting a pyramid shape. This phenomenon is a characteristic of the CSAM process, attributed to the velocity profile of the particles during the deposition; the particles in the core achieve greater velocity, promoting more deposition in the center of the jet than in its periphery [35].

In the Figs. 7 and 8 the profiles of the Ti patterned coatings produced with both powders (Ti-I and Ti-S) are shown with their corresponding microstructures, using squared patterns of two distinct dimensions (3×3 mm and 1.5×1.5 mm, respectively).

In the case of the 3×3 mm pattern, the pin fins of both powders were coated with an identical number of layers (Fig. 7) in order to study the effect of the deposition efficiency of the powder in the final characteristics of the deposit. As observed in Fig. 7, squared pin fins of big dimensions were obtained using this pattern. Despite being sprayed with

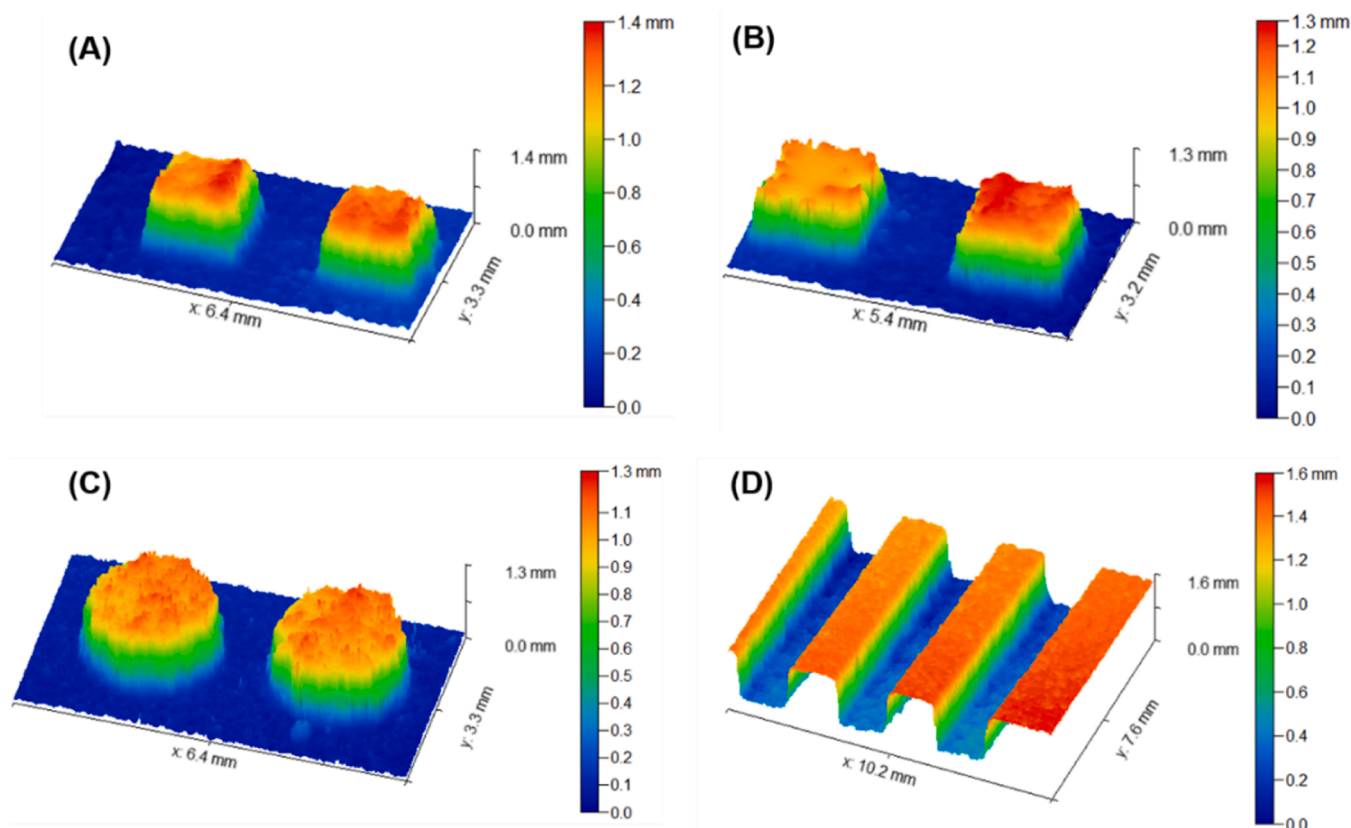


Fig. 6. 3D topography of different CSAM BPPs patterns. (A) Ti-S small squares, (B) Ti-I small squares, (C) Ti-I cylinders, (D) Ti-S rows.

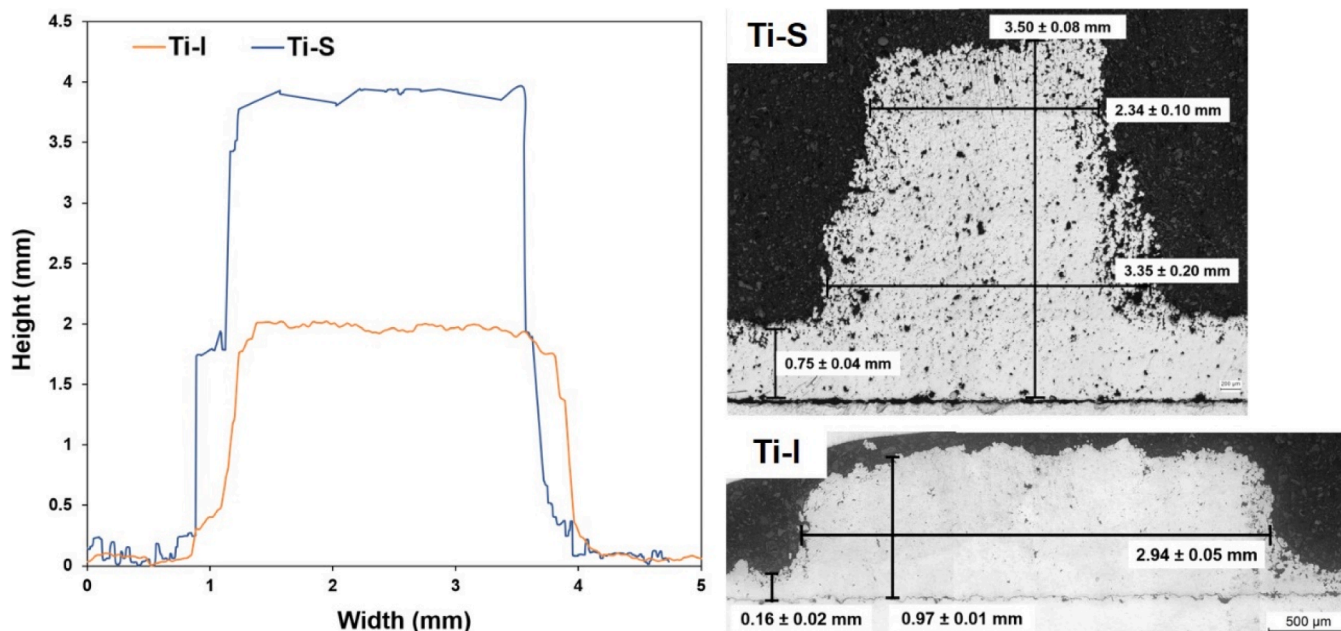


Fig. 7. Profiles and cross-sectional optical microscope (OM) surface images of the 3D big squared patterns of the CSAM BPPs.

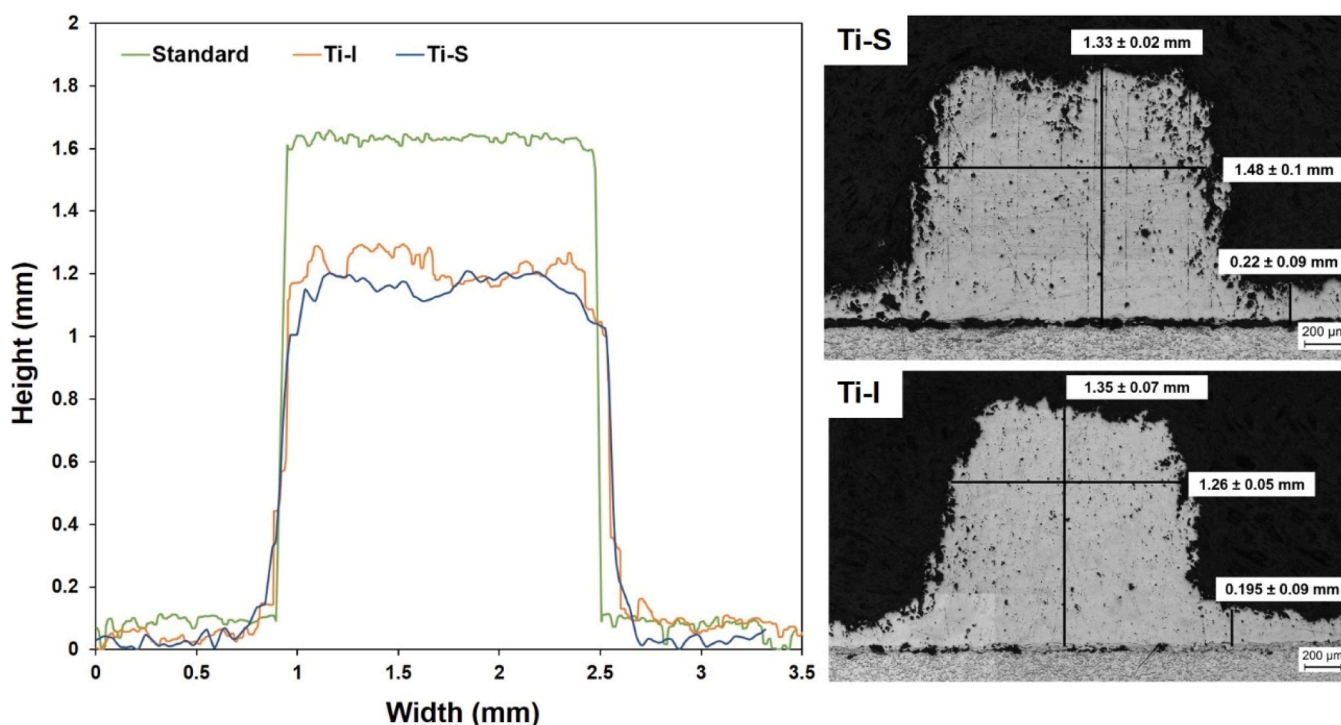


Fig. 8. Profiles and cross-sectional optical microscope (OM) surface images of the 3D small squared patterns of the CSAM BPPs compared to a commercial standard.

the same layers, powder Ti-S was shown to almost double the height of powder Ti-I. This difference is attributed to their distinct morphologies; as mentioned before, spherical powders are known to have a higher deposition efficiency than irregular powders [30,36]. Therefore, under the same parameters, the morphology of the powder directly influences the total height of the Ti 3D coatings.

Fig. 8 exhibits the 3D profiles of the Ti coatings produced with a 1.5×1.5 mm pattern. In this case, number of deposition layer adjustments were made to attain a height comparable to a commercial standard BPP. The profiles of the 3D coatings (Fig. 8) revealed that the width and

height of the pin fins can be tailored with accuracy based on the dimensions of the inverse pattern cut in the mask.

In the same way, the cross-sectional microstructure of the squared patterns of powders Ti-I and Ti-S are also shown in Figs. 7-8. Overall, it was observed that the width of all the samples was consistent with the dimensions of the mesh. For the big squares (Fig. 8A-B), a mesh with voids of 3×3 mm was used, leading to a width of the pins of 2.94 ± 0.05 mm for Ti-I, and 2.34 ± 0.10 mm for Ti-S. Furthermore, the small squares (Fig. 8C-D) showed similar results; for the mesh with squared voids of 1.5×1.5 mm, the pins showed a width of 1.26 ± 0.05 mm (Ti-I)

and 1.48 ± 0.10 mm (Ti-S). This revealed that even though there was some interference of the mesh with the particle deposition, the pins grew with similar dimensions as the voids in the masks. Consistently with the 3D topography, the tendency of all powders to form pins with a pyramid shape was also observed.

Moreover, the sprayed Ti deposits showed a higher superficial roughness than the commercial BPP. This rough surface is very common in CSAM deposits due to the impact of the particles. Hence, to ensure adequate contact of the BPPs inside the electrolyzer cell, post-process step to reduce the superficial roughness is recommended.

3.3. Microstructure, mechanical properties & adhesion

In addition to the dimensional characteristics of the BPPs, the evaluation of their microstructure is very important, as intrinsic defects like cracks or pores may be present. To minimize these defects, the selected spraying parameters need to be optimized. Although CS is a suitable technology to process Ti, the literature reports challenges in obtaining dense parts, with porosities reported to be as high as 20 % [37].

Table 3 shows the microstructural results for porosity, roughness, microhardness, and adhesion strength of the Ti-S and Ti-I small squares. In particular, the powder Ti-S presented a slightly higher porosity (6 ± 1 %) compared to the irregular powder (4 ± 1 %). These results are consistent with the work of Wong et al. [30] in which the porosity of several CS Ti coatings was evaluated based on powder morphology, resulting in porosity values of 3 % and 5 % for irregular and spherical powders, respectively. It is worth indicating that in all cases, a denser microstructure is exhibited in the center of the pins than on the edges. This may be attributed to the interference of the mesh with the in-flight particles, as well as to a lack of tampering effect of subsequent particles in these walls. This phenomenon has also been observed in other works that studied the masked CSAM process [25,38]. For instance, Cormier et al. [25] characterized Al and SS 316 L pyramidal fin arrays manufactured with masked CSAM. Their findings revealed that the Al fins presented a porosity distribution in which the core resulted denser than the exterior layers. However, the SS 316 L fins exhibited a homogeneous porosity. The authors attributed this difference to the bonding characteristics of both powders; the core Al particles were more prone to compaction by the impact of the subsequent particles compared to SS 316L. In the same way, cold sprayed Ti coatings are well known to be sensitive to this tampering effect, typically Ti deposits exhibit a porosity distribution in the first layers tend to be denser compared to the external layers [37].

As mentioned before, both powders presented a high superficial roughness of $Ra 17 \pm 2$ μm and $Rz 78 \pm 6$ μm for Ti-I, and $Ra 16 \pm 4$ μm and $Rz 67 \pm 9$ μm for Ti-S. These values could affect negatively the conductivity needed in the cell due to a poor contact between the BPPs and the GDL. For this reason, a post-process step is recommended to ensure a close contact between all elements in the PEM electrolyzer stack.

Another significant aspect when manufacturing BPPs with CSAM is the adhesion of the patterned coatings to the substrate. An inadequate adhesion of the 3D pattern can impede an efficient functionality of the plates. The bonding strength between the sprayed powders and the substrate was evaluated, revealing that both of them exhibited cohesive failures at 59 ± 2 MPa for Ti-I, and 45 ± 5 MPa for Ti-S, indicating a proper bonding strength between the coating and the substrate.

In general terms, CSAM is an efficient method capable of processing

Table 3
Microstructural characteristics & adhesion of the small squares pin fins.

Sample	Porosity (%)	Roughness (Ra, Rz - μm)	Microhardness (HV _{0.2})	Adhesion (MPa)
Ti-I	4 ± 1	(17 ± 2 , 78 ± 6)	171 ± 17	59 ± 2
Ti-S	6 ± 1	(16 ± 4 , 67 ± 9)	193 ± 23	45 ± 5

titanium in its solid state, making it possible to produce BPPs with customized flow-fields within a few minutes and to overcome the challenges of other traditional methods such as stamping or machining. The masked technology allowed to customize the size and shape of the flow fields by adjusting the quantity of layers sprayed and the patterns of the mesh.

3.4. Electrochemical experiments

To ensure a long-term durability and efficient functioning of the electrolyzer, a fundamental requisite for the BPPs is their inherent resistance to corrosion. In particular, the anodic side of the plate is subjected to an aggressive chemical acidic environment originating from the electrochemical reactions responsible for the splitting of the water molecules [4]. Only a limited number of materials have the characteristics to effectively operate at such conditions. Laedre et al. [4] studied the corrosion properties and ICR of non-coated materials at the conditions experienced in a PEM water electrolyzer. These materials included Mo, W, SS 316 L, SS 304 L, IN625, Nb, Ta, and Ti. This study revealed that, among these materials, Nb, Ta, and Ti demonstrated an excellent corrosion resistance. However, after prolonged polarizations their ICR was significantly increased. Langemann et al. [39] designed a set of experiments to determine candidate coating materials for SS 304 BPPs, based on their resistance to corrosion under the pH conditions found in an operating PEM water electrolyzer. It was found that under high potentials the pH value dropped significantly in the anode side of the electrolyzer. Under these conditions the authors proposed Au and TiN as coatings solutions for corrosion resistance enhancement, however even Au and TiN coated components revealed signs of corrosion after exposition to 0.5 M H₂SO₄ solution. Conversely, Lettenmeier et al. [40] coated SS BPPs with Ti by Vacuum Plasma Spraying (VPS) which was subsequently top-coated with Pt by magnetron sputtering Physical Vapor Deposition (PVD). The assessment of the Pt-coated BPPs in a commercial PEM electrolyzer for 1000 h revealed that the duplex Pt-Ti coatings fully protected the SS substrate, while achieving an excellent cell durability.

In this work, the CSAM Ti BPPs were tested as a basis for determining its resistance to corrosion without a top coating. A bulk Ti plate was also tested for comparative reasons. For this, corrosion measurements were performed with a three-electrode cell in the range potential of -0.1 V to 1.8 V vs Ag/AgCl, which is the potential range that can be found in an operating PEM electrolyzer cell. Fig. 9 shows the polarization curves

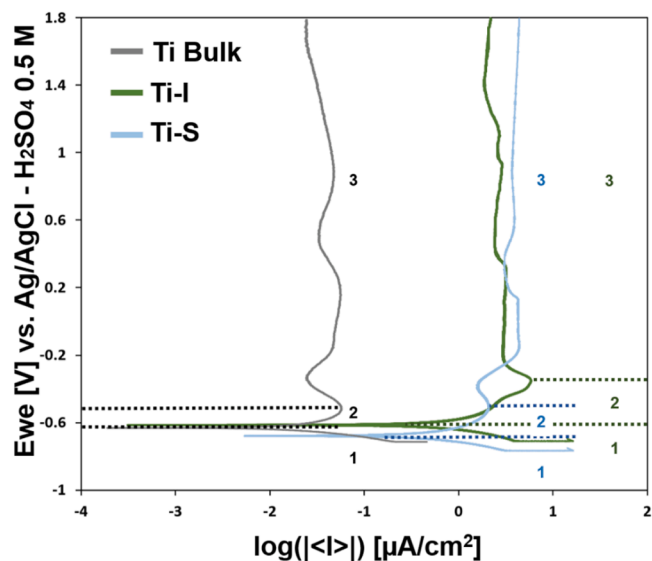


Fig. 9. Polarization curves showing electrochemical stages (1) cathodic, (2) active zone, (3) passivation processes.

recorded, while Table 4 shows the corrosion resistance results E_{corr} and I_{corr} .

The polarization curves were recorded in the range potential of -0.1 V to 1.8 V vs Ag/AgCl to study the stability of the oxide film formed in the surface of the samples during the anodic corrosion. Of the three different zones typically observed for the corrosion processes (1. cathodic region, 2. active zone, and 3. passivation processes), the last two represent the anodic behavior of the samples [13].

All the tested samples showed an active zone (zone 2), representing the point at which the corrosion current reaches its maximum point before starting the passivation processes. Samples Ti-S and the Ti Bulk showed a subtle active peak, while the Ti-I exhibited a more prolonged active zone to higher current densities. Following the active zone, an oxide film began to form on the surface of all samples, inducing material passivation. This protective film caused a drop in the corrosion current, which remained stable until the potential reached 1.8 V. For some materials, during this passivation region (zone 3) the oxide film can break, causing a steep rise in the corrosion current, generating pitting corrosion [41]. None of the materials tested in this study exhibited this behavior, hence their oxide films are stable enough within the operating potential range of a PEM electrolyzer.

As for the corrosion potential E_{corr} results, shown in Table 4, all samples exhibited similar values; -614 ± 9 mV for Ti-I, -665 ± 14 mV for Ti-S, and -640 ± 17 mV for the Ti Bulk. Similar corrosion current densities to those reported by Laedre et al. [4] for Ti plates were measured for the new Ti CSAM surfaces. Despite of this, a clear difference in the I_{corr} between the Ti CSAM powders and the Ti Bulk, with values of 250 ± 14 $\mu\text{A}/\text{cm}^2$ for Ti-I, 220 ± 10 $\mu\text{A}/\text{cm}^2$ for Ti-S, and 15 ± 4 $\mu\text{A}/\text{cm}^2$ for the Ti Bulk, was observed. As expected, the bulk exhibited a better resistance to corrosion than the manufactured BPPs by CSAM. These values are consistent with the results obtained by Laedre et al. [4] on the potentiostatic tests; current densities of 170 $\mu\text{A}/\text{cm}^2$ for the Ti plates were reported.

In terms of corrosion rate, the samples presented values of $2.2 \times 10^{-3} \pm 1.2 \times 10^{-4}$ mm/yr, $1.9 \times 10^{-3} \pm 8.8 \times 10^{-5}$ mm/yr, and $1.3 \times 10^{-4} \pm 3.5 \times 10^{-5}$ mm/yr, for samples Ti-I, Ti-S, and Ti Bulk, respectively. This behavior may be attributed to intrinsic defects within the microstructure of the CSAM BPPs, particularly to the increased porosity of the sprayed parts in comparison with the Bulk plate. Two mechanisms responsible of this phenomenon are well documented in the literature, Hussain et al. [41] investigated the role of porosity in the corrosion behavior of CS Ti coatings, observing a decreased corrosion resistance of the as-sprayed Ti Coatings with 11 % of interconnected porosity due to the percolation of the electrolyte through the pores towards the substrate, causing galvanic corrosion. Moreover, Ahmed et al. [42] studied the effects of porosity in corrosion resistance of thermal sprayed coatings. The results indicated that the non-interconnected porosity led to crevice corrosion in the pores, which negatively impacted the corrosion performance. Based on these findings, it is more likely that the second phenomenon—crevice corrosion within non-interconnected pores—is occurring in the Ti-I and Ti-S samples, since the reduced porosity (approximately 50 % lower than that reported by Hussain et al.) in both CSAM Ti samples likely prevents the percolation of the electrolyte to the substrate.

To determine the stability of the Ti surfaces produced by CSAM, the samples were immersed in a 0.5 M H_2SO_4 solution and subjected to a constant potential of 2 V for 100 h. Fig. 10 shows the E_{corr} and I_{corr} results before and after the post-mortem tests for all the samples. In

Table 4
Corrosion resistance results.

Sample	E_{corr} (mV)	I_{corr} ($\mu\text{A}/\text{cm}^2$)	Corrosion rate (mm/yr)
Ti-I	-614 ± 9	250 ± 14	$2.2 \times 10^{-3} \pm 1.2 \times 10^{-4}$
Ti-S	-665 ± 14	220 ± 10	$1.9 \times 10^{-3} \pm 8.8 \times 10^{-5}$
Ti Bulk	-640 ± 17	15 ± 4	$1.3 \times 10^{-4} \pm 3.5 \times 10^{-5}$

particular, the Ti-Bulk maintained its corrosion resistance values before and after the post-mortem tests. However, the two cold-sprayed Ti coatings showed higher E_{corr} and lower I_{corr} values, attributed to the formation of a stable and thick superficial oxide layer which is clearly affecting the electrochemical response of the surface and, which appearance is consistent with the behavior of both materials shown in the polarization curves in Fig. 9. This stable protective layer allows for these Ti surfaces deposited by CSAM to perfectly withstand the aggressive conditions of the electrolyzer cell without corroding however it might have a detrimental effect in their final electrical conductivities.

3.5. Interfacial contact resistance

Since PEM water electrolyzers require an energy input, the electrical resistance of the entire cell must be as low as possible for it to operate at its maximum efficiency. It has been shown that the most critical point for ohmic losses is at the point of contact between the BPP and the gas diffusion layer [43]. Therefore, the electrical resistance of the plates must be maintained as low as possible.

Fig. 11 shows the results of the interfacial contact resistance tests at different compaction forces, based on the approach of Wang et al. [26].

The ICR values for all materials diminished as higher compaction pressures were applied, which is attributed to an enhancement in the superficial contact area. In general, the Ti Bulk demonstrated lower ICR values compared to both Ti patterned surfaces produced with Ti-I and Ti-S powders by CSAM. This shift is attributed to the inherent defects present in the CSAM process, such as pores and inter-particle boundaries. On the other hand, no important differences in the ICR values were found between the CS powders, which suggests that the electrical conductivity is determined by the nature of the material and not the morphology of the powder. Particularly, at a compaction pressure of 150 N/cm² ICR values of 42 ± 19 , 40 ± 13 , and 24 ± 7 m Ω ·cm² were obtained for Ti-I, Ti-S, and Ti Bulk, respectively; all of these values are consistent with other studies found in the literature [44,45]. Although these values are higher than what the DOE target sets (ICR < 10 m Ω ·cm² at 140 N/cm²), CSAM is still a feasible process for the production of BPPs.

Another key property of the BPPs is their ability to maintain their electrically conductive properties at the same time as they maintain their resistance to corrosion. Fig. 12 compares ICR values for all the samples before and after the 100 h post-mortem tests.

In all cases, after the post-mortem tests, there was a notable increase in the ICR, indicating that the oxide layer formed on the surface impeded the conductivity of the specimens after 100 h, in agreement with the results observed in the electrochemical tests. This effect was more evident in the CSAM samples, in which the permeation of H_2SO_4 through the superficial pores may have contributed to a more pronounced corrosion, decreasing the electrical conductivity of the BPPs. In future studies, strategies to address the decrease of the ICR value for CSAM BPPs are encouraged, for example, the application of PVD coatings [15].

4. Conclusions

This study establishes an efficient methodology for the production of Bipolar Plates using the Cold Spray Additive Manufacturing technology with customized flow-fields within a few minutes, overcoming the challenges of other traditional methods such as stamping or machining. To summarize, the following key findings can be concluded:

- The masked CSAM process allowed to manufacture Ti BPPs with customized flow-fields within a few minutes. The produced pin fins that make of the flow-fields were homogeneous, presenting the same shape and size: the mesh with voids of 3×3 mm lead to a width of the pins of 2.94 ± 0.05 mm for Ti-I, and 2.34 ± 0.10 mm for Ti-S, while the mesh with squared voids of 1.5×1.5 mm, resulted in

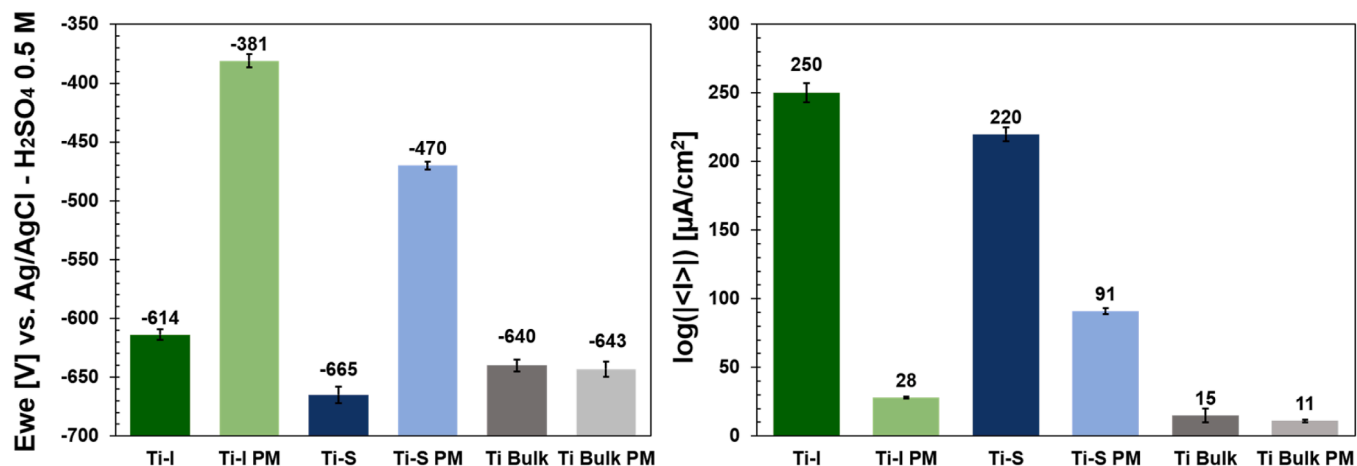


Fig. 10. Corrosion resistance results before and after the post-mortem tests.

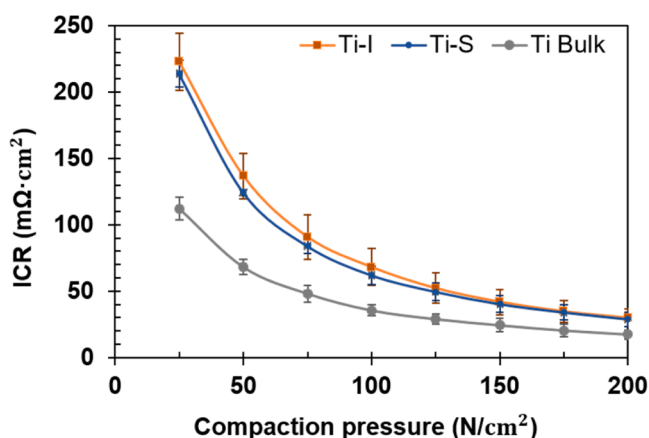


Fig. 11. Interfacial contact resistance at different compaction pressures.

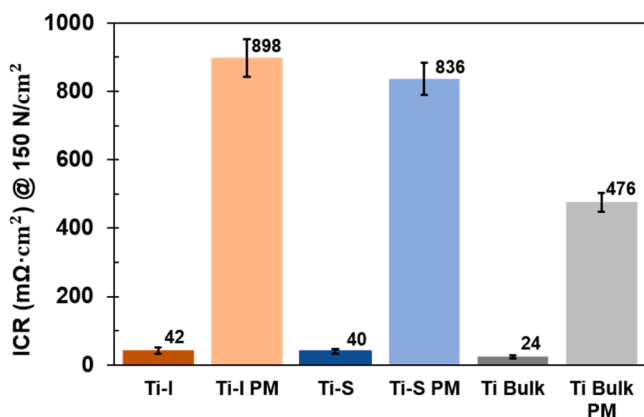


Fig. 12. Interfacial contact resistance at 150 N/cm² before and after the post-mortem tests.

pins with a width of 1.26 ± 0.05 mm for Ti-I and 1.48 ± 0.10 mm for Ti-S.

- The CSAM Ti BPPs presented porosity values of 6 ± 1 % and 4 ± 1 % for powders Ti-S and Ti-I, respectively. Both deposits exhibited a high superficial roughness, hence a final post-processing step is suggested to ensure a good contact of the BPP in the cell.
- The evaluation of the corrosion resistance of the CSAM Ti patterned coatings showed that for both Ti-S and Ti-I powders a stable oxide

film at the typical operation potential (1.8 V vs Ag/AgCl) of a PEM water electrolyzer was formed. No signs of pitting corrosion were observed in the range of potentials under assessment confirming the high stability and resistance of these Ti surfaces to acidic environments.

- At a compaction pressure of 150 N/cm² ICR values of 42 ± 19 , 40 ± 13 , and 24 ± 7 were obtained for Ti-I, Ti-S, and Ti Bulk, respectively. Furthermore, after the post-mortem tests, there was a notable increase in the ICR, indicating that the oxide layer formed on the surface impeded the conductivity of the specimens.
- The morphology of the powder only has an influence on the deposition efficiency. The resistance to corrosion and ICR properties are dependent on the nature of the material. Therefore, using an irregular powder contributes to a cost-effective manufacturing of BPPs.

5. Funding

Author A. Garfias would like to thank AGAUR for grant 2021 FISDU 00300. This work is part of the project TED2021-130461B-I00, funded by MICIU/AEI/10.13039/501100011033 and by the European Union "NextGenerationEU"/PRTR. V. Albaladejo-Fuentes is a Serra Hunter Fellow,

CRedit authorship contribution statement

Andrea Garfias: Writing – original draft, Investigation, Formal analysis, Data curation. **María Sarret:** Validation, Resources, Methodology, Formal analysis. **Javier Sánchez:** Validation, Project administration, Methodology, Conceptualization. **Irene G. Cano:** Writing – review & editing, Supervision, Resources, Project administration, Methodology, Formal analysis. **Vicente Albaladejo-Fuentes:** Writing – review & editing, Supervision, Project administration, Methodology, Funding acquisition, Formal analysis, Conceptualization. **Teresa Andreu:** Writing – review & editing, Project administration, Funding acquisition, Conceptualization.

Declaration of competing interest

The authors declare the following financial interests/personal relationships which may be considered as potential competing interests:

Vicente Albaladejo Fuentes has patent pending to University of Barcelona. If there are other authors, they declare that they have no known competing financial interests or personal relationships that could have appeared to influence the work reported in this paper.

Data availability

The authors do not have permission to share data.

References

- [1] P.P. Edwards, V.L. Kuznetsov, W.I.F. David, Hydrogen energy, *Philos. Trans. R. Soc. A: Math. Phys. Eng. Sci.* 365 (2007) 1043–1056, <https://doi.org/10.1098/rsta.2006.1965>.
- [2] A.Z. Arsal, M.A. Hannan, A.Q. Al-Shetwi, M. Mansur, K.M. Muttaqi, Z.Y. Dong, et al., Hydrogen energy storage integrated hybrid renewable energy systems: a review analysis for future research directions, *Int. J. Hydrogen. Energy* 47 (2022) 17285–17312, <https://doi.org/10.1016/j.ijhydene.2022.03.208>.
- [3] M. Carmo, D.L. Fritz, J. Mergel, D. Stolten, A comprehensive review on PEM water electrolysis, *Int. J. Hydrogen. Energy* 38 (2013) 4901–4934, <https://doi.org/10.1016/j.ijhydene.2013.01.151>.
- [4] S. Lædre, O.E. Kongstein, A. Oedegaard, H. Karoliussen, F. Seland, Materials for proton exchange membrane water electrolyzer bipolar plates, *Int. J. Hydrogen. Energy* 42 (2017) 2713–2723, <https://doi.org/10.1016/j.ijhydene.2016.11.106>.
- [5] S. Dunn, Hydrogen futures: toward a sustainable energy system, *Int. J. Hydrogen. Energy* 27 (2002) 235–264, [https://doi.org/10.1016/S0360-3199\(01\)00131-8](https://doi.org/10.1016/S0360-3199(01)00131-8).
- [6] A. Ursúa, L.M. Gandía, P. Sanchis, Hydrogen production from water electrolysis: current status and future trends, in: *Proceedings of the IEEE*, 100, Institute of Electrical and Electronics Engineers Inc., 2012, pp. 410–426, <https://doi.org/10.1109/JPROC.2011.2156750>.
- [7] S.A. Grigoriev, V.N. Fateev, D.G. Bessarabov, P. Millet, Current status, research trends, and challenges in water electrolysis science and technology, *Int. J. Hydrogen. Energy* 45 (2020) 26036–26058, <https://doi.org/10.1016/j.ijhydene.2020.03.109>.
- [8] Q. Meng, X. Yue, L. Shang, X. Liu, F. Wang, G. Zhang, Corrosion behavior of metallic coatings on titanium bipolar plates of proton exchange membrane water electrolysis, *Int. J. Hydrogen. Energy* 63 (2024) 1105–1115, <https://doi.org/10.1016/j.ijhydene.2024.03.242>.
- [9] X. Luo, C. Ren, J. Song, H. Luo, K. Xiao, D. Zhang, et al., Design and fabrication of bipolar plates for PEM water electrolyser, *J. Mater. Sci. Technol.* 146 (2023) 19–41, <https://doi.org/10.1016/j.jmst.2022.10.039>.
- [10] A. Tang, L. Crisci, L. Bonville, J. Jankovic, An overview of bipolar plates in proton exchange membrane fuel cells, *J. Renew. Sustain. Energy* 13 (2021), <https://doi.org/10.1063/5.0031447>.
- [11] S. Porstmann, T. Wannemacher, W.G. Drossel, A comprehensive comparison of state-of-the-art manufacturing methods for fuel cell bipolar plates including anticipated future industry trends, *J. Manuf. Process.* 60 (2020) 366–383, <https://doi.org/10.1016/j.jmapro.2020.10.041>.
- [12] F. Dundar, E. Dur, S. Mahabunphachai, M. Koç, Corrosion resistance characteristics of stamped and hydroformed proton exchange membrane fuel cell metallic bipolar plates, *J. Power. Sources.* 195 (2010) 3546–3552, <https://doi.org/10.1016/j.jpowsour.2009.12.040>.
- [13] M.J.K. Lodhi, K.M. Deen, W. Haider, Corrosion behavior of additively manufactured 316L stainless steel in acidic media, *Materialia* (Oxf) 2 (2018) 111–121, <https://doi.org/10.1016/j.mta.2018.06.015>.
- [14] W. Yoon, X. Huang, P. Fazzino, K.L. Reifsnider, M.A. Akkaoui, Evaluation of coated metallic bipolar plates for polymer electrolyte membrane fuel cells, *J. Power. Sources.* 179 (2008) 265–273, <https://doi.org/10.1016/j.jpowsour.2007.12.034>.
- [15] H. Sun, K. Cooke, G. Eitzinger, P. Hamilton, B. Pollet, Development of PVD coatings for PEMFC metallic bipolar plates, *Thin. Solid. Films.* 528 (2013) 199–204, <https://doi.org/10.1016/j.tsf.2012.10.094>.
- [16] A. Baroutaji, A. Arjunan, J. Robinson, M.A. Abdulkareem, A.G. Olabi, Additive manufacturing for Proton Exchange Membrane (PEM) hydrogen technologies: merits, challenges, and prospects, *Int. J. Hydrogen. Energy* 52 (2024) 561–584, <https://doi.org/10.1016/j.ijhydene.2023.07.033>.
- [17] K.S. Lyons, B.D. Gould, Lightweight titanium metal bipolar plates for PEM fuel cells, in: *Materials Science Forum*, 879, Trans Tech Publications Ltd, Switzerland, 2017, pp. 613–618, <https://doi.org/10.4028/www.scientific.net/MSF.879.613>.
- [18] S. Celik, B. Timurkutluk, U. Aydin, M. Yagiz, Development of titanium bipolar plates fabricated by additive manufacturing for PEM fuel cells in electric vehicles, *Int. J. Hydrogen. Energy* 47 (2022) 37956–37966, <https://doi.org/10.1016/j.ijhydene.2022.08.282>.
- [19] C. Romero, D. Benedetto, E. Gordo, Processing and surface modification of titanium open cell porous structures for PEM fuel cell bipolar plates, *Int. J. Hydrogen. Energy* 52 (2023) 1190–1201, <https://doi.org/10.1016/j.ijhydene.2023.06.287>.
- [20] H. Ye, Z. Tu, S. Li, Electrochemical performance of metal nitride coated titanium bipolar plate for proton exchange membrane water electrolyser, *J. Power. Sources.* 595 (2024), <https://doi.org/10.1016/j.jpowsour.2024.234052>.
- [21] G. Yang, J. Mo, Z. Kang, F.A. List, J.B. Green, S.S. Babu, et al., Additive manufactured bipolar plate for high-efficiency hydrogen production in proton exchange membrane electrolyzer cells, *Int. J. Hydrogen. Energy* 42 (2017) 14734–14740, <https://doi.org/10.1016/j.ijhydene.2017.04.100>.
- [22] G. Yang, S. Yu, J. Mo, Z. Kang, Y. Dohrmann, F.A. List, et al., Bipolar plate development with additive manufacturing and protective coating for durable and high-efficiency hydrogen production, *J. Power. Sources.* 396 (2018) 590–598, <https://doi.org/10.1016/j.jpowsour.2018.06.078>.
- [23] P. Huang, Z. Chen, J. Zhang, M. Wu, Y. Liu, F. Zhang, et al., Stainless steel bipolar plate fuel cell with different flow field structures prepared by laser additive manufacturing, *Int. J. Heat. Mass Transf.* 183 (2022), <https://doi.org/10.1016/j.ijheatmasstransfer.2021.122186>.
- [24] M. Sánchez-Molina, E. Amores, N. Rojas, M. Kunowsky, Additive manufacturing of bipolar plates for hydrogen production in proton exchange membrane water electrolysis cells, *Int. J. Hydrogen. Energy* 46 (2021) 38983–38991, <https://doi.org/10.1016/j.ijhydene.2021.09.152>.
- [25] Y. Cormier, P. Dupuis, B. Jodoin, A. Corbeil, Net shape fins for compact heat exchanger produced by cold spray, *J. Therm. Spray Technol.* 22 (2013) 1210–1221, <https://doi.org/10.1007/s11666-013-9968-x>.
- [26] H. Wang, M.A. Sweikart, J.A. Turner, Stainless steel as bipolar plate material for polymer electrolyte membrane fuel cells, *J. Power. Sources.* 115 (2003) 243–251, [https://doi.org/10.1016/S0378-7753\(03\)00023-5](https://doi.org/10.1016/S0378-7753(03)00023-5).
- [27] D.P. Davies, P.L. Adcock, M. Turpin, S.J. Rowen, Bipolar plate materials for solid polymer fuel cells, *J. Appl. Electrochem.* 30 (2000) 101–105, <https://doi.org/10.1023/A:1003831406406>.
- [28] IRENA. Green hydrogen cost reduction: scaling up electrolyzers to meet the 1.5 °C #n: scaling up electrolyzers to meet the 1.5 °C climate GOAL, 2020.
- [29] R.F. Vaz, A. Silvello, J. Sanchez, V. Albaladejo, I. Garcia-Cano, The influence of the powder characteristics on 316L stainless steel coatings sprayed by cold gas spray, *Coatings* 11 (2021) 1–18, <https://doi.org/10.3390/coatings11020168>.
- [30] W. Wong, P. Vo, E. Irissou, A.N. Ryabinin, J.G. Legoux, S. Yue, Effect of particle morphology and size distribution on cold-sprayed pure titanium coatings, *J. Therm. Spray Technol.* 22 (2013) 1140–1153, <https://doi.org/10.1007/s11666-013-9951-6>.
- [31] S. Porstmann, T. Wannemacher, W.G. Drossel, A comprehensive comparison of state-of-the-art manufacturing methods for fuel cell bipolar plates including anticipated future industry trends, *J. Manuf. Process.* 60 (2020) 366–383, <https://doi.org/10.1016/j.jmapro.2020.10.041>.
- [32] F.K. Chen, K.H. Chiu, Stamping formability of pure titanium sheets, *J. Mater. Process. Technol.* 170 (2005) 181–186, <https://doi.org/10.1016/j.jmatprotec.2005.05.004>.
- [33] X. Li, I. Sabir, Review of bipolar plates in PEM fuel cells: flow-field designs, *Int. J. Hydrogen. Energy* 30 (2005) 359–371, <https://doi.org/10.1016/j.ijhydene.2004.09.019>.
- [34] S. Karimi, N. Fraser, B. Roberts, F.R. Foulkes, A review of metallic bipolar plates for proton exchange membrane fuel cells: materials and fabrication methods, *Adv. Mater. Sci. Eng.* 2012 (2012), <https://doi.org/10.1155/2012/828070>.
- [35] A. Garfias, R. Vaz, V. Albaladejo-Fuentes, J. Sánchez, I.G. Cano, Geometry and microstructure control of remanufactured metallic parts by cold spray additive manufacturing, *Materials* (Basel) 16 (2023) 4735, <https://doi.org/10.3390/ma16134735>.
- [36] M.F. Morks, S.H. Zahiri, J. Lang, X.B. Chen, S. Gulizia, I.S. Cole, The influence of powder morphology on the microstructure and mechanical properties of as-sprayed and heat-treated cold-sprayed CP Ti, *Int. J. Adv. Manuf. Technol.* 118 (2022) 3869–3881, <https://doi.org/10.1007/s00170-021-08222-9>.
- [37] W. Li, C. Cao, S. Yin, Solid-state cold spraying of Ti and its alloys: a literature review, *Prog. Mater. Sci.* 110 (2020), <https://doi.org/10.1016/j.pmatsci.2019.100633>.
- [38] P. Dupuis, Y. Cormier, M. Fenech, B. Jodoin, Heat transfer and flow structure characterization for pin fins produced by cold spray additive manufacturing, *Int. J. Heat. Mass Transf.* 98 (2016) 650–661, <https://doi.org/10.1016/j.ijheatmasstransfer.2016.03.069>.
- [39] M. Langemann, D.L. Fritz, M. Müller, D. Stolten, Validation and characterization of suitable materials for bipolar plates in PEM water electrolysis, *Int. J. Hydrogen. Energy* 40 (2015) 11385–11391, <https://doi.org/10.1016/j.ijhydene.2015.04.155>.
- [40] P. Lettenmeier, R. Wang, R. Abouatallah, F. Burggraf, A.S. Gago, K.A. Friedrich, Coated Stainless Steel Bipolar Plates for Proton Exchange Membrane Electrolyzers, *J. Electrochem. Soc.* 163 (2016) F3119–F3124, <https://doi.org/10.1149/2.014161jes>.
- [41] T. Hussain, D.G. McCartney, P.H. Shipway, T. Marrocco, Corrosion behavior of cold sprayed titanium coatings and free standing deposits, *J. Therm. Spray Technol.* 20 (2011) 260–274, <https://doi.org/10.1007/s11666-010-9540-x>.
- [42] N. Ahmed, M.S. Bakare, D.G. McCartney, K.T. Voisey, The effects of microstructural features on the performance gap in corrosion resistance between bulk and HVOF sprayed Inconel 625, *Surf. Coat. Technol.* 204 (2010) 2294–2301, <https://doi.org/10.1016/j.surfcoat.2009.12.028>.
- [43] P. Jendras, K. Lötsch, T. Von Unwerth, Requirements and testing methods for surfaces of metallic bipolar plates for low-temperature PEM fuel cells, in: *IOP Conf Ser Mater Sci Eng*, 181, Institute of Physics Publishing, 2017, <https://doi.org/10.1088/1757-899X/181/1/012018>.
- [44] H. Zhang, M. Hou, G. Lin, Z. Han, Y. Fu, S. Sun, et al., Performance of Ti-Ag-deposited titanium bipolar plates in simulated unitized regenerative fuel cell (URFC) environment, *Int. J. Hydrogen. Energy* 36 (2011) 5695–5701, <https://doi.org/10.1016/j.ijhydene.2011.01.154>.
- [45] S. Lædre, O.E. Kongstein, A. Oedegaard, F. Seland, H. Karoliussen, Measuring in situ interfacial contact resistance in a proton exchange membrane fuel cell, *J. Electrochem. Soc.* 166 (2019) F853–F859, <https://doi.org/10.1149/2.1511912jes>.